Energy Conversion Efficiency Assessment of a Direct Drive Wave Energy Converter with Different Current Controllers

Hugo Mendonça

Sergio Martinez

I. Introduction

As a renewable energy source, electricity generation from wave energy is continuously attracting research and development efforts worldwide. Hundreds of companies [1] are working in diverse wave energy converters (WEC) at different development phases [2]. Many WECs of different types use the relative movement between two bodies to drive the electrical generator, in general, with intermediate mechanical or hydraulic energy conversions. Some types of WECs, as the Archimedes Wave Swing [3] or the Uppsala/Seabed AB [4], submerged and floating oscillating bodies, respectively, according to [5], make use of a direct coupling between the moving parts and the power take off (PTO) system, typically a linear permanent magnet synchronous generator (PMSG), to improve conversion efficiency and reliability. The electrical energy generated by a linear PMSG depends on the linear speed of the moving part, the translator, which in turn depends on the buoy motion. Due to the nonregular, oscillating nature of ocean waves, there is no sinusoidal steady state in the generated electricity, and direct drive systems require power electronics to interface with the electrical grid.

Different power electronics topologies and control strategies have been developed to improve the efficiency of WECs [6].

This work was supported in part by CAPES, Coordination for he Improvement of Higher Level Personnel (Brazil), under Grant BEX-9376135 and in part by the Spanish Ministry of Economy and Competitivity under Grant ENE2012-36981.

From a theoretical point of view, the power absorbed by a WEC is maximal when the buoy velocity is in phase with the excitation force. As there is no direct control on the floating body, the maximum can be reached by acting on the PTO force. In direct drive systems, the generator-side converter can be used to improve the WEC efficiency by acting on the PMSG load force. The objective of the work described in this paper is to assess the performance of a three-phase fully-controlled generator-side converter, according to the resistance emulation method presented in [7], with three different current control strategies as in [8], but from the point of view of conversion efficiency.

Section II of the paper describes the WEC model used in the work. Section III summarizes the main characteristics of the generator, and the control strategies and filtering implemen- tation under study. Sections IV and V present the simulation results and conclusions.

II. WEC Model

The WEC under study in this work is a point absorber consisting of a cylindrical buoy limited to heave motion and rigidly connected to a PTO system (a linear PMSG) on the seabed, as it is schematically shown in Fig. 1. A detailed model of the WEC and its dynamic behavior are described in [7], [9]. As the PTO nonlinearities do not affect the magnitudes of interest in this work, they have been neglected for simplicity. The motion of the buoy can be described by the Cummins equation [10]:

$$[m + A(\infty)] \cdot \ddot{y}(t) + \int_{-\infty}^{t} k_r(t-\tau) \cdot \dot{y}(t)\, d\tau + \rho g S_w \cdot y(t) = f(t) \quad (1)$$

where $y(t)$, m, $A(\infty)$, ρ, g, and S_w stand for: vertical displacement, mass, added mass at high frequency, fluid density,

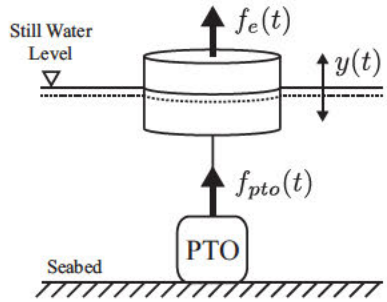

Fig. 1. Schematic representation of a wave energy point absorber.

acceleration due to gravity, and water plane area. The integral term in equation 1, the fluid memory, is given by [11]:

$$k_r(t) = \int_0^\infty B(\omega)\cos(\omega t)\,\mathrm{d}\omega \tag{2}$$

where $B(\omega)$ is the potential damping. The external forces on the buoy can be expressed as $f(t) = f_e(t) + f_{pto}(t)$ (Fig. 1), where the excitation force caused by the incoming waves can be calculated as:

$$f_e(t) = \int_{-\infty}^\infty k_e(t)\zeta(t-\tau)\,\mathrm{d}\tau \tag{3}$$

where $\zeta(t)$ is the elevation of the sea surface and $k_e(t)$ is the non-causal impulse response function (IRF) of the wave excitation, that can be calculated by the inverse Fourier transform of the wave-to-force RAO (Response Amplitude Operator), as shown in [12]. The added mass, the potential damping and the wave-to-force RAO are hydrodynamic parameters given in the frequency domain and they are usually calculated by boundary elements methods available in a few commercial softwares, such as AQWA and WAMIT [13]. The PTO force, f_{pto}, is the electromagnetic force induced between the stator and the translator of the linear PMSG. This electromagnetic force is given as a function of the current [9], so it can be controlled by a current control technique.

III. The Generator-Side Converter

As the generator voltage is variable in amplitude and frequency, the interface with the grid is achieved in two stages: the generator-side converter (ac-dc) and the grid-side converter (dc-ac). Fig. 2 illustrates the whole system where the grid side has been simply modeled as a dc source because its behavior is not of interest in this study. Apart from the ac-dc conversion, the generator-side part is where the PTO force can be controlled in order to improve the WEC efficiency. This work focus on the optimization method presented in [7] where the PTO force is controlled by adjusting the current at the generator terminals. This method consists on connecting a three-phase optimal resistive load that best matches the wave characteristics. This idea is illustrated in Fig. 3, where R_{op} is the optimal value of the resistance that should be connected to the linear PMSG to improve its efficiency. In fact, there is no physical resistor as shown in Fig. 3, but rather a power electronic system that is able to emulate such resistance. Fig. 2 represents the resistance emulation system, where the linear PMSG is connected to a boost-rectifier.

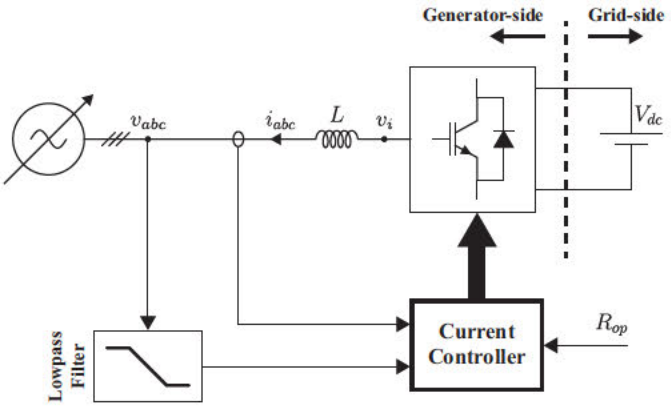

Fig. 2. Resistance emulation system.

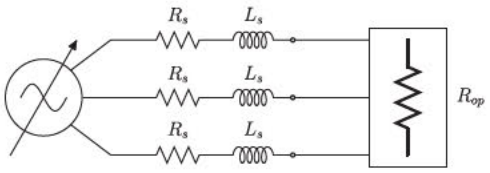

Fig. 3. Ideal model in the generator side.

A. Linear PMSG

Similar to a rotating synchronous generator, the linear PMSG output voltage can be modeled in the rotating dq frame as:

$$v_d = R_s i_d + \frac{\mathrm{d}\lambda_d}{\mathrm{d}t} - \omega\lambda_q \tag{4a}$$

$$v_q = R_s i_q + \frac{\mathrm{d}\lambda_q}{\mathrm{d}t} + \omega\lambda_d \tag{4b}$$

where R_s is the armature resistance; i_d and i_q are the currents in the dq frame; $\lambda_d = L_s i_d + \lambda_{PM}$ and $\lambda_q = L_s i_q$ are the winding flux linkages, where L_s is the synchronous inductance and λ_{PM} is flux linkage produced by the translator magnets; and $\omega = \pi\dot{y}/\tau_p$, being τ_p the pole pitch. This work assumes that the translator's length is infinite, i.e., the active area of the stator is always constant.

B. Current Controllers

As the control principle is based on emulating the resistance R_{op}, the phase voltages at the generator terminals must be proportional to the line currents. In simple words, this means that the current is controlled to be in phase with the phase voltage. So, in this case, the PTO force can be controlled directly by a current controller and its current reference signals are calculated from the phase voltage measurements as:

$$\boldsymbol{i^*_{abc}} = \frac{\boldsymbol{v_{abc}}}{R_{op}} \tag{5}$$

where $\boldsymbol{v_{abc}} = \begin{bmatrix} v_{an} & v_{bn} & v_{cn} \end{bmatrix}$ is a vector with the phase voltages at the generator terminals. The implementation of

the current controllers depend on the system requirements and many strategies have been applied to power electronic circuits, as it can be seen in [14]. In this work, three current control strategies are compared: Hysteresis-Band Current Control (HBCC), Space-Vector PWM Current Control (SVPWMCC) and Spatial Hysteresis Current Source Control (SHCSC). The current reference direction adopted in this work is the one going out of the boost-rectifier, as shown in Fig. 2.

1) Hysteresis-band current control: This is a straightforward strategy where the measured current signals at the generator terminals track the current references within a hysteresis band, β. For this control scheme, one independent controller per phase is used, as shown in Fig. 4 for phase a. The switching signals are produced when the error between the current reference signal and the measured current exceeds the hysteresis band, i.e., when $i_a^* - i_a > \beta/2$, then Q_1 is on. On the other hand, when $i_a^* - i_a < -\beta/2$, Q_4 is on. This method has a very good dynamic performance. However, a few drawbacks can be mentioned, such as unpredictable switching frequency, redundancy of one hysteresis controller and no intercommunication between the individual hysteresis controllers.

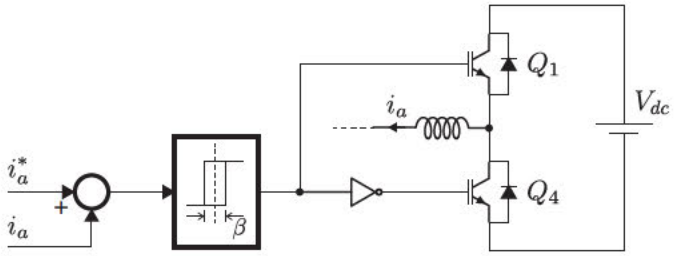

Fig. 4. Hysteresis-band current controller.

2) Space-Vector PWM current control: In this control strategy, a voltage source converter (VSC) is used to set a voltage at the boost-rectifier terminals to provide the required current. So, the terminal voltages of the generator-side converter v_i in dq frame (Fig. 2) are:

$$v_{id} = R_s \cdot i_d + (L_s + L) \cdot \frac{\mathrm{d}i_d}{\mathrm{d}t} - \omega(L_s + L) \cdot i_q \qquad (6a)$$

$$v_{iq} = R_s \cdot i_q + (L_s + L) \cdot \frac{\mathrm{d}i_q}{\mathrm{d}t} - \omega \cdot [(L_s + L) \cdot i_d + \lambda_{PM}] \qquad (6b)$$

where L is the filter inductance between the linear PMSG and the boost-rectifier. The implementation of this control model is shown in Fig. 5, where the measured currents are transformed into the dq frame components and they are compared with the dq current reference signals that are generated, similarly to equation 5, as follow:

$$\boldsymbol{i_{dq}^*} = \frac{\boldsymbol{v_{dq}}}{R_{op}} \qquad (7)$$

where $\boldsymbol{v_{dq}} = \begin{bmatrix} v_d & v_q \end{bmatrix}$. The error signals go to proportional-integral (PI) controllers in two channels whose outputs are added to the cross-coupling terms, resulting in the voltage references to the VSC. From these references, the switching of the boost-rectifier can be determined by a Space Vector Modulation (SVM) technique [15]. Compared to the HBCC, this method has the advantage of having a determinate switching frequency. On the other hand, PI controllers are usually tuned at an operating point which is constantly changing in the case of WECs, since the voltage frequency changes with the wave frequency. Thus, the dynamic response of the WEC is also conditioned by the dynamics of the PI controllers.

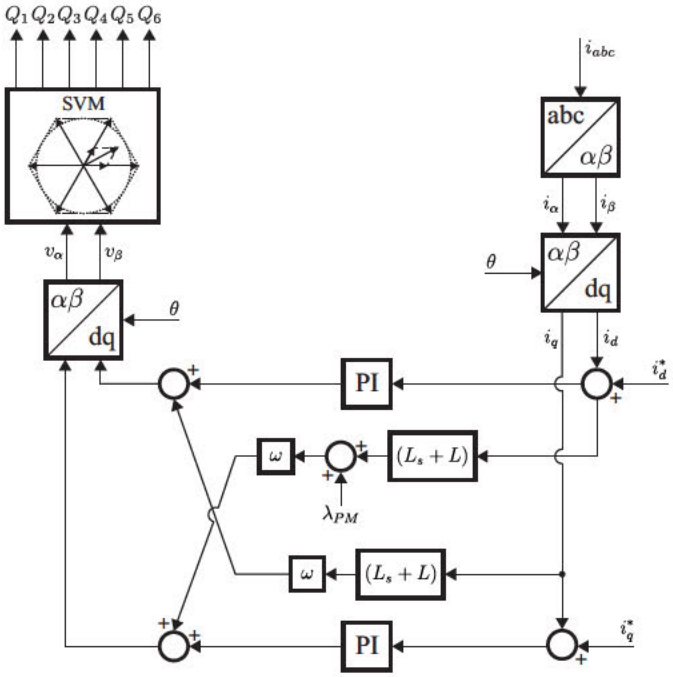

Fig. 5. Space-Vector PWM current controller.

3) Spatial hysteresis current source control: This controller, described in [16], uses a nonlinear current source and a SVM, combining the advantages of both HBCC and SVPMWCC. In other words, it presents a very good response independent of parameter changes and a constant switching frequency. Instead of independent hysteresis-band controllers per phase, a single circular space area at the end of the current space vector is used. So, during each cycle of the SVM, the voltage space phasor of the inverter is calculated to make the actual current space phasor get closer to the position of the reference current space phasor, within the aforementioned circular hysteresis band. This control scheme is shown in Fig. 6.

C. Low-Pass Filter

The voltage at the generator terminals is pulsed due to the switching of the converter. As the voltage measurements are used to generate the current reference signals, the voltage signals must be filtered to eliminate the high frequency harmonic components. For this purpose, a low-pass filter is used as shown in Fig. 2. Within a range of different filter types, this work evaluates two of them:

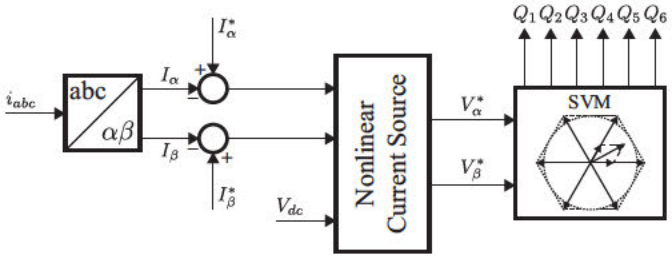

Fig. 6. Spatial hysteresis current source controller.

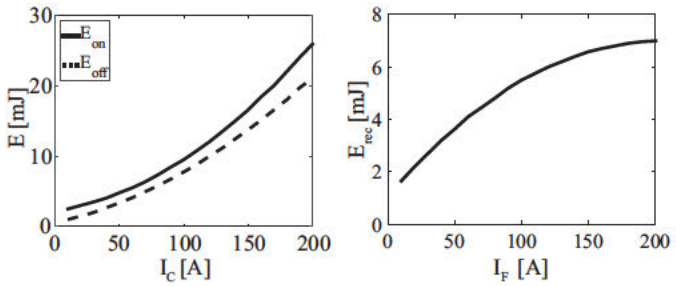

(a) IBGT. (b) Diode.

Fig. 7. Typical curves of inverter switching losses for $V_{CE} = 120\,\text{V}$ and $T_{jv} = 125°\text{C}$ (IGBT-modules FF100R12KS4 [18]).

- A first order filter:

$$H(s) = \frac{1}{1 + \tau \cdot s} \tag{8}$$

where s is the Laplace operator, $\tau = \frac{1}{2\pi f_c}$, f_c being the cutoff frequency.

- A second order filter:

$$H(s) = \frac{\omega_n^2}{s^2 + 2\zeta\omega_n \cdot s + \omega_n^2} \tag{9}$$

where $\omega_n = \frac{1}{2\pi f_n}$, f_n is the natural frequency, and ζ is the damping ratio.

IV. Energy Efficiency Assessment

As it can be seen in [8], the filtered voltage at the generator terminals has high frequency harmonic components that, for example, in the case of the HBCC, make it operate with a high switching frequency. So, the low-pass filter plays a key role in the WEC performance. To evaluate how the voltage low-pass filter affects the power delivered to the grid-side converter for each current controller considered in this work, the system in Fig. 2 is simulated with the low-pass filters presented in Section III-C.

A. Simulation Parameters

The system is simulated with a ten minutes wave date series mathematically generated from the modified two-parameter Pierson-Moskowitz spectrum [17] whose statistical parameters are the significant height $H_s = 2\,\text{m}$ and the energy period $T_e = 8\,\text{s}$. For these statistical parameters, the optimal resistance is $R_{op} = 1.3\,\Omega$ that is kept constant. The inductance of the series inductor filter between the linear PMSG and the boost-rectifier is $L = 20\,\text{mH}$. The rated power of the linear PMSG is 10 kW with $\tau_p = 50\,\text{mm}$, $R_s = 0.44\,\Omega$, $L_s = 11.7\,\text{mH}$ and nominal voltage $V = 200\,\text{V}$ at 0.7 m/s. The translator weighs 1000 kg and, assuming that its maximum speed is 1.5 m/s, the maximum electrical frequency of the generated voltage is 15 Hz. The HBCC has the hysteresis band set to $\beta = 2\,\text{A}$ and both SVPWMCC and SHCSC have the switching frequency, f_{sw}, set to 5 kHz.

In addition, the boost rectifier is composed of an IGBT module whose nominal values: collector-emitter voltage $V_{CE} = 1200\,\text{V}$ and collector current $I_C = 100\,\text{A}$. To compute the total switching losses, both IBGT and diode switching losses must be taken into account. The IGBT switching losses are the sum of all turn-on and turn-off energies described as $E = f(I_c, T_{jv})$, where T_{jv} is the junction temperature of the module, so these energies can be taken from Fig. 7a. On the other hand, in the case of the diode, only the recovery energy counts and it is described as $E_{rec} = f(I_F, T_{jv})$, where I_F is the dc forward current. The recovery energy can be taken from Fig. 7b. Therefore, the total switching losses can be calculated as:

$$P_{sw} = (E_{on} + E_{off}) \cdot f_{sw} + E_{rec} \cdot f_{sw} \tag{10}$$

B. Simulation Results

First, to introduce a base value for comparison, the ideal model (presented in Fig. 3) has been simulated and the average power delivered to the resistive load R_{op} was 4.28 kW. Then, the system shown in Fig. 2 has been simulated with a first order low-pass filter whose cutoff frequency is varied from 20 Hz to 300 Hz. The current obtained for each current controller is compared to the ideal current as shown in Fig. 8 for the cutoff frequencies 20 and 200 Hz. It is expected that the more frequency harmonic components are filtered, more phase shift is introduced. This statement can be verified in Fig. 8 for all of the three current controllers, where, for $f_c = 20\,\text{Hz}$, the current presents a greater phase shift than for $f_c = 200\,\text{Hz}$. Besides, the phase shift is mainly introduced when the wave frequency is higher. However, from the point of view of current waveform quality, the lower cutoff frequency, the better current quality.

From the point of view of energy conversion efficiency, Fig. 9 shows the average power delivered to the grid-side converter taking into account the converter switching losses (equation 10) in a ten minutes period, for the three current controllers under study. The SVPWMCC shows a higher level of injected power compared to the other controllers for $f_c > 70\,\text{Hz}$. Smaller cutoff frequencies result in higher efficiency for the SHCSC. In both controllers, SVPWMCC and SHCSC, the average switching losses remain almost constant with cutoff frequency.

On the other hand, in the case of the HBCC, both cutoff and switching frequencies play an important role in power terms resulting in an optimal operation point as it can be verified in Fig. 9. The fact that the current reference signal presents

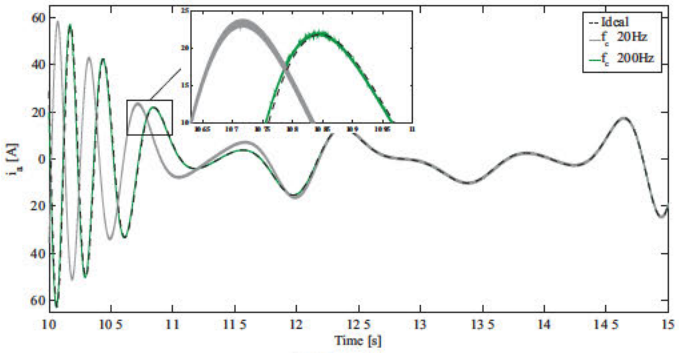

(a) HBCC.

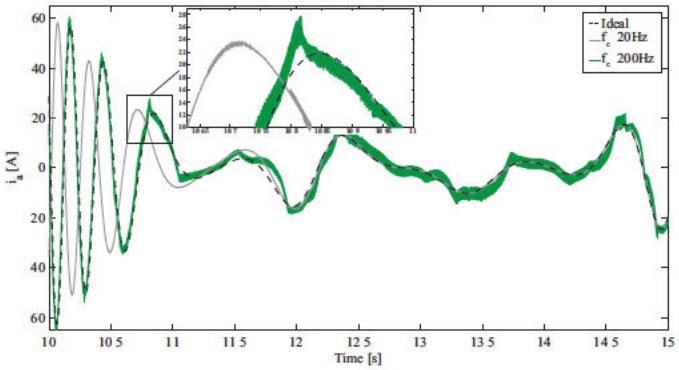

(b) SVPWMCC.

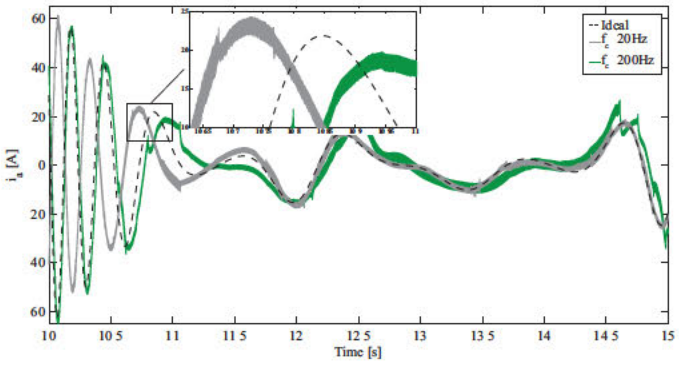

(c) SHCSC.

Fig. 8. Line currents in phase-a for the ideal system and for the resistance emulation system with a first order low-pass filter.

more harmonic oscillation for higher cutoff frequencies results in a oscillating hysteresis band, as shown in [8], that, in turn, increases the switching frequency and also the switching losses. This effect can be verified in Fig. 10, where the distribution of the switching frequencies with respect to each cutoff frequency is shown. For $f_c = 200\,\text{Hz}$, the converter has a very high switching frequency, about 20 kHz, even close to impractical values. This is the reason why the current quality is as good as for $f_c = 20\,\text{Hz}$, even presenting smaller ripple. Note that in both cases the hysteresis band is not respected. Decreasing the cutoff frequency, the switching frequency also decreases and is more concentrated around one value.

Fig. 11 shows the ideal current compared with the current obtained from the system in Fig. 2 for the case of the second

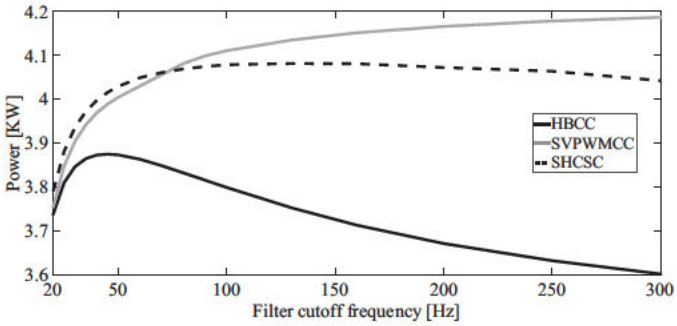

Fig. 9. Power delivered to the grid-side converter as a function of the cutoff frequency with a first order low-pass filter.

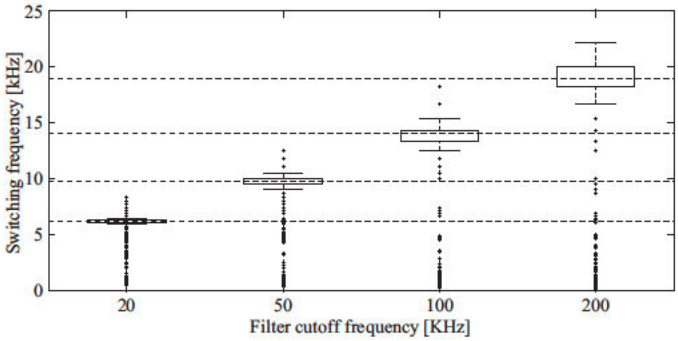

Fig. 10. Distribution of switching frequency with respect to the cutoff frequency for the case of SHCSC.

order low-pass filter. It can be seen that there is no great difference in the current quality for all of the implemented controllers. The SVPWMCC has the smallest ripple, while the SHCSC the highest. Now, it is possible to verify that, in the case of the HBCC, the hysteresis band is respected and, no matter the filter natural frequency, the switching frequency remains practically constant around 3 kHz and almost constant for the three controllers (5 kHz for the SVPWMCC and SHCSC). The power delivered to the grid-side converter just varies with the filter natural frequency, as shown in Fig. 12. The delivered power decrease for smaller natural frequency is due to the phase shift introduced by the filter that results in incorrect current reference signals. Despite keeping a right proportionality between voltage and current, it makes them be out of phase. In general, the three controllers provide almost the same power and it is clear that, in the case of the second order filter, the natural frequency must be set to values greater than 200 Hz. Beyond this value, for the three controllers, the maximum deviation with respect to the power delivered by the ideal model is 4%.

V. Conclusion

In this work, three different current controllers have been implemented to emulate an optimal resistance that improves the WEC efficiency. Keeping this optimal resistance constant, the performance of the system is evaluated from the point of view of the power delivered to the grid-side converter.

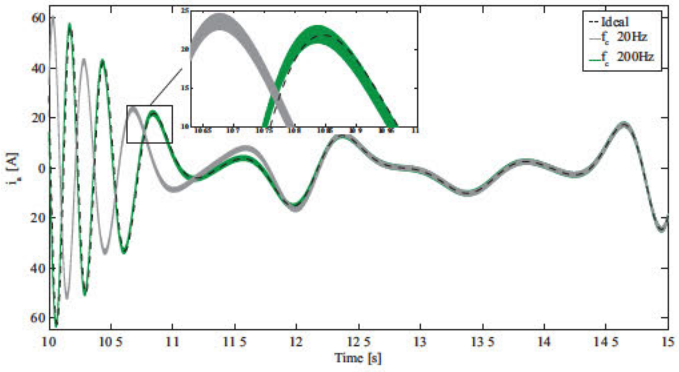

(a) HBCC.

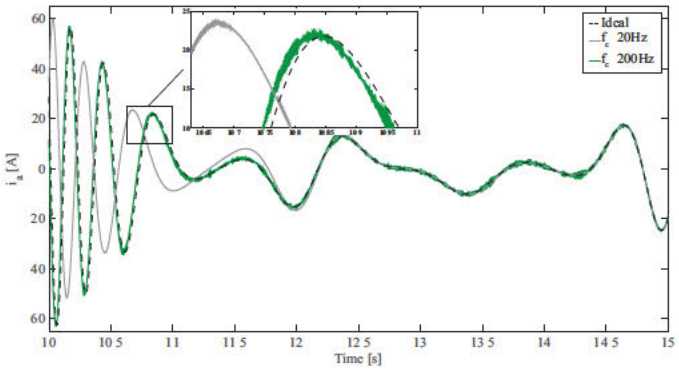

(b) SVPWMCC.

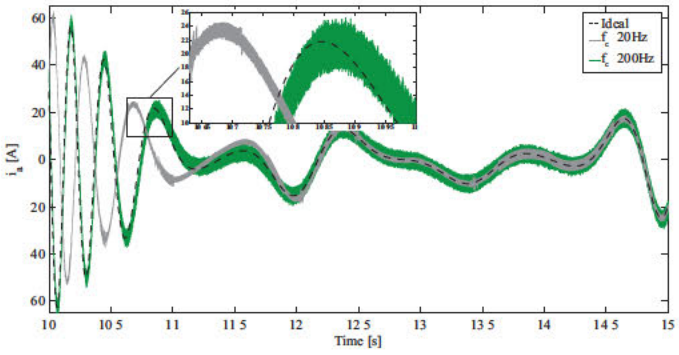

(c) SHCSC.

Fig. 11. Line currents in phase-a for the ideal system and for the resistance emulation system with a second order low-pass filter.

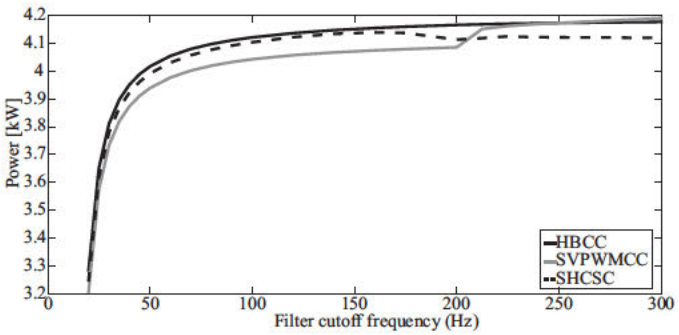

Fig. 12. Power delivered to the grid-side converter as a function of the cutoff frequency with a second order low-pass filter.

The delivered power is also assessed according to the voltage low-pass filter configuration. Actually, it is verified that the filter plays an important role in this system, since the quality and accurace of the reference signal generated by the current controller depends on the filtered voltage. The results presented in this study suggest that the implementation of a second order filter with natural frequency above 200 Hz, but sufficiently below the high frequency harmonic components generated by the converter. In addition, in this configuration, the three current controllers present a good current quality with the SVPWMCC presenting the smallest ripple.

REFERENCES

[1] EMEC - The European Marine Energy Centre. [Online]. Available: http://www.emec.org.uk/marine-energy/wave-developers/

[2] I. López, J. Andreu, S. Ceballos, I. M. de Alegría, and I. Kortabarria, "Review of wave energy technologies and the necessary power-equipment," *Renewable and Sustainable Energy Reviews*, vol. 27, pp. 413–434, 2013.

[3] H. Polinder, M. E. Damen, and F. Gardner, "Linear pm generator system for wave energy conversion in the AWS," *Energy Conversion, IEEE Transactions on*, vol. 19, no. 3, pp. 583–589, 2004.

[4] M. Leijon, C. Boström, O. Danielsson, S. Gustafsson, K. H. O. Langhamer, E. Strömstedt, M. Stålberg, J. Sundberg, O. Svensson, S. Tyrberg, and R. Waters, "Wave energy from the north sea: Experiences from the lysekil research site," *Surveys in Geophysics*, vol. 29, pp. 221–240, 2008.

[5] A. F. O. Falcão, "Wave energy utilization: A review of the technologies," *Renewable and sustainable energy reviews*, vol. 14, no. 3, pp. 899–918, 2010.

[6] J. Ringwood, G. Bacelli, and F. Fusco, "Energy-maximizing control of wave-energy converters: The development of control system technology to optimize their operation," *Control Systems, IEEE*, vol. 34, no. 5, pp. 30–55, 2014.

[7] H. Mendonca and S. Martinez, "A resistance emulation approach to optimize the wave energy harvesting for a direct drive point absorber," *Sustainable Energy, IEEE Transactions on*, vol. 7, no. 1, pp. 3–11, 2016.

[8] H. Mendonca, S. Martinez, and D. Ramirez, "Comparison of current control strategies applied to a boost-rectifier connected to a direct drive wave energy converter," in *Renewable Energy Research and Application (ICRERA), 2015 International Conference on*. IEEE, to be published.

[9] H. Mendonca and S. Martinez, "Modeling of a wave energy converter connected to a resistive load," in *Energy (IYCE), 2013 4th International Youth Conference on*. IEEE, 2013, pp. 1–6.

[10] W. Cummins, "The impulse response function and ship motions," *Schiffstechnik*, vol. 9, pp. 101–109, 1962.

[11] E. Kristiansen and O. Egeland, "Frequency-dependent added mass in models for controller design for wave motion damping," in *Manoeuvring and control of marine craft 2003 (MCMC 2003): a proceedings volume from the 6th IFAC Conference, Girona, Spain, 17-19 September*, 2003.

[12] J. Falnes, "On non-causal impulse response functions related to propagating water waves," *Applied Ocean Research*, vol. 17, no. 6, pp. 379–389, 1995.

[13] B. Bosma, Z. Zhang, T. K. Brekken, H. Özkan-Haller, C. McNatt, and S. C. Yim, "Wave energy converter modeling in the frequency domain: A design guide," in *Energy Conversion Congress and Exposition (ECCE), 2012 IEEE*. IEEE, 2012, pp. 2099–2106.

[14] M. P. Kazmierkowski and L. Malesani, "Current control techniques for three-phase voltage-source pwm converters: a survey," *Industrial Electronics, IEEE Transactions on*, vol. 45, no. 5, pp. 691–703, 1998.

[15] Z. Yu, "Space vector PWM with TMS 320C24x/F24x using hardware and software determined switching patterns," *Texas Instruments Report SPRA524*, March 1999.

[16] D. Ramirez, S. Martinez, C. Carrero, and C. A. Platero, "Improvements in the grid connection of renewable generators with full power converters," *Renewable Energy*, vol. 43, pp. 90–100, 2012.

[17] The Specialist Committee on Waves (chaired by C. T. Stansberg), "Final report and recommendations to the 23rd ITTC," in *Proceedings of the 23rd International Towing Tank Conference*, vol. II, 2002, pp. 505–551.

[18] Infineon, "FF100R12KS4 data sheet," October 2013.